Thermal Analysis on Plume Heating of the Main Engine
on the Crew Exploration Vehicle Service Module

Xiao-Yen J. Wang and James R.Yuko
Thermal/Fluids System Branch
NASA Glenn Research Center
Cleveland, OH 44135

Abstract

The crew exploration vehicle (CEV) service module (SM) main engine plume heating is analyzed using multiple numerical tools. The chemical equilibrium compositions and applications (CEA) code is used to compute the flow field inside the engine nozzle. The plume expansion into ambient atmosphere is simulated using an axisymmetric space-time conservation element and solution element (CE/SE) Euler code, a computational fluid dynamics (CFD) software. The thermal analysis including both convection and radiation heat transfers from the hot gas inside the engine nozzle and gas radiation from the plume is performed using Thermal Desktop. Three SM configurations, Lockheed Martin (LM) designed 604, 605, and 606 configurations, are considered. Design of multilayer insulation (MLI) for the stowed solar arrays, which is subject to plume heating from the main engine, among the passive thermal control system (PTCS), are proposed and validated.

1. Introduction

The CEV service module will experience heating from the rocket engine when the engine is firing during phases of the mission, such as the circularization burn to orbit and the trans-earth injection. The main engine and its plume could get extremely hot and will radiate significant heat to its adjacent components on the SM. The stowed solar panel is next to the engine nozzle and becomes the major concern. Thermal analysis is performed to compute the temperature on the solar panel due to the heat from both the main engine and its plume. Proper thermal MLI blanket design for the solar panel is also proposed and validated to keep the panel under its maximum safe operating temperature limits.

In the following, the simulation of the flow field inside the engine nozzle and its plume expansion into ambient atmosphere are described first, which is followed by the thermal analysis performed using Thermal Desktop.

2. Simulation of flow inside the engine nozzle and its plume

As the first step, the CEA code is used to compute the engine performance. The flow properties, such as the pressure p, density ρ, velocity V, temperature T, and mole fractions of the exhaust gas at the injector and the end of the combustor, nozzle throat, and nozzle exit, are also obtained. The thermodynamic properties of the exhaust gas provided by CEA code are used to compute the heat transfer coefficient inside the engine nozzle with the empirical equations in [1]. The flow properties at the nozzle exit and the thermodynamic properties are used in the CFD simulation of the plume expansion into the ambient air. The gas radiation from the hot exhaust gas is computed using a simplified engineering approach

described in [2]. Each topic will be described in detail and numerical results are reported as follows.

2.1 Service module main engine performance

The thermodynamic and flow properties of the flow inside the main engine are computed using CEA code. Given the key engine parameters, such as the chamber pressure, oxidizer and fuel names and their ratio, chamber subtraction and expansion area ratios, propellant mass flow rate as the CEA inputs, the CEA computes the properties at different locations inside the thrust chamber and the results are listed in Table 1. At the nozzle exit, the mole fractions of the exhaust species based on chemical equilibrium are 33.56% of H_2O, 13.6% of CO_2, 3.22% of CO, 32.8% of N_2, and 16.9% of H_2, which will be used in the plume radiation calculation.

Table 1 Engine performance (CEA results)

	Injector	Combustion end	Throat	Exit
p, BAR	8.6	8.07	4.81	0.00457
T, K	3137	3124	2967.8	915.6
ρ, kg/m^3	0.7092	0.6673	0.4237	0.001347
sonic velocity, m/s	1175.6	1172.7	1137.3	651.8
Mach number	0	0.244	1	5.082

2.2 Convective heat transfer inside the engine nozzle

A steady-state one-dimensional model for isentropic flows of an ideal gas through a converging-diverging nozzle is used to compute the flow variables of the hot gas inside the engine nozzle along the axial direction. The convective heat transfer coefficient that is a function of Reynolds and Prandtl numbers based on empirical equations [1] can be computed. Figure 1 show the computed heat transfer coefficient and temperature of hot gas along the flow direction, which will be used later in the thermal analysis.
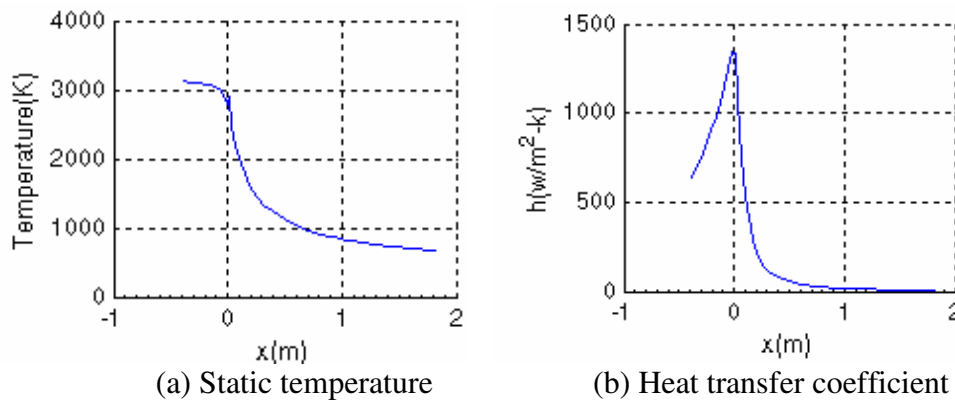

(a) Static temperature   (b) Heat transfer coefficient

Figure 1 Heat transfer coefficient and hot gas temperature inside the nozzle.

2.3 Engine plume expansion into the ambient

The exhaust plume is simulated using a CFD code, the CE/SE two-dimensional/axisymmetric Euler solver. An ideal gas is assumed and the exhaust gas properties at the nozzle exit obtained from CEA is used. Two altitudes (100 and 400 km) at the angle of attack α (= 0°) that is the angle between the vehicle velocity and thrust vectors are considered. At the inlet of the computational domain (nozzle exit), we define

$$p = 0.0045 \text{ atm}, \ T = 915.6 \text{ K}, \ \rho = 1347 \text{ kg/m}^3, \ u = 3.312 \text{ km/s}, \ v = 0.0 \text{ km/s}$$

It should be pointed out that the nozzle cone half angle 20° at the exit of the chamber is not included here. The ambient conditions are

$$p = p_a, \ \rho = \rho_a, \ u = V \cos \alpha, \ v = V \sin \alpha$$

where p_a and ρ_a are the pressure and density of the ambient air, respectively, and V = 7.8 km/s is the vehicle velocity. For the 400 km altitude, the CFD code becomes unstable due to numerical issues related to very small density and pressure at that altitude. The code can produce converged plume results up to 100 km altitude. To approximate the ambient air condition at 400 km altitude and above, the pressure and density of the ambient air at the altitude of 100 km with zero air velocity are used. It results in zero dynamic pressure ($\rho_a V^2$) of the ambient air and gives a reasonable approximation to the ambient condition at 400 km altitude and above since $\rho_a V^2$ (= 0.00017 N/m^2) at the altitude of 400 km is very small. The ambient air conditions at different altitudes are listed in Table 2.

Table 2 the ambient air conditions at different altitudes

Altitude (m)	Temperature (K)	Pressure (atm)	Density (kg/m^3)
100,000	195.08	3.16E-07	5.60E-07
200,000	845.56	8.36E-10	2.54E-10
400,000	995.83	1.43E-11	2.80E-12

The computed numerical results are plotted in Figures 2 and 3. In Figure 2, $\log_{10} \rho$, $\log_{10} p$, temperature contours and plume relative to CEV are plotted for 100 km altitude at α = 0°. The corresponding plume pattern for the altitude of 400 km and above is plotted in Figure 3. The air shock, exhaust shock, and air/exhaust mixing are seen in the plume at the altitude of 100 km, which agrees with some plume patterns shown in [3]. The major mass is within the plume intrinsic core near the nozzle exit. No shock waves are observed in the plume and the plume expands more at 400 km altitude. For the vacuum case, the exhaust gas expands to reach the Prandtl-Meyer limit that is 103° [4] including the half cone angle of 20°. However, the major mass is still within the intrinsic core. The altitude has negligible effect on the intrinsic core.

2.4 Gas radiation computation

Considering the gas radiation, strong emission by carbon dioxide (CO_2) and water vapor (H_2O) (polar molecules) is in infrared (IR) region and weaker emission is in the ultraviolet

(UV) and visible ranges. Non-polar gases such as O_2, N_2, and H_2, do not emit radiation and are transparent to incident thermal radiation. The approach for computing the gas radiation presented in [2] is used here and will be described briefly in the following.

The radiation heat flux $q = A_s \varepsilon_g \sigma T_g^4$, where A_s is the surface area, σ is Stephan-Boltzmann constant, ε_g is the gas emissivity, correlated in terms of gas temperature T_g, total pressure p of the gas, partial pressure p_g of the radiating species, and mean beam length Le = 4 V_s/A_s with V_s being the volume. Furthermore

$$\varepsilon_g = \varepsilon_c + \varepsilon_w - \Delta\varepsilon$$

where ε_w is the emissivity of H_2O, ε_c is the emissivity of CO_2, and $\Delta\varepsilon$ is the correction term for H_2O and CO_2 mixing. The partial pressure of CO_2 and H_2O are computed as

$$p_{CO2} = p\, m_{CO2}, \quad p_{H2O} = p\, m_{H2O}$$

where m_{CO2} and m_{H2O} are the mole fractions of CO_2 and H_2O, respectively. The data of ε_w, ε_c, and $\Delta\varepsilon$ can be found in [2].

For the flow inside the engine nozzle, since the flow properties change drastically along the flow direction, the hot gas is split into three parts along the axial direction x to calculate the radiation heat flux. Each part is defined using its starting and ending x locations, denoted as x_s and x_e, respectively. Table 3 lists the geometry of the three parts and the corresponding results of the heat flux. Note that the regenerative cooling is not included here.

Table 3 Radiation heat flux inside the nozzle

$[x_s, x_e]$ (m)	height (m)	volume (m^3)	surface area (m^2)	Le (m)	$p_{CO2}Le$ (atm-ft)	$p_{H2O}Le$ (atm-ft)	ε_g	T_g (K)	q (kw)
[0, 0.5]	0.5	0.1	0.864	0.466	0.454	1.122	0.207	2050	179
[0.5,1.0]	0.5	0.417	1.8059	0.92456	0.011	0.0275	0.0074	1050	0.92
[1.0,1.8]	0.8	1.7171	4.52	1.52	0.00427	0.0105	0.0024	950	0.5

The so-computed radiation heat flux for the plume is listed in Tables 4 and 5 for 100 and 400 km altitudes, respectively. The volume-averaged gas pressure and temperature are used in the calculation. Since the regenerative cooling in the engine nozzle is not considered, the actual exhaust gas temperature will be lower. For the 100 km altitude, the plume core is split into three right circular cones (shown in Figure 2(b)) based on the pressure contour. Each right circular cone is defined using its top and bottom radius denoted as r_1 and r_2 and the height. Thus the corresponding surface area and volume can be computed. The radiation due to the interaction between the exhaust and ambient air is not calculated here. For 400 km and above altitudes, the plume core is split into two right circular cylinders (shown in Figure 3(b)). The radiation due to the interaction between ambient air and exhaust gas is negligible due to the high altitude.

The radiation from both the rocket nozzle and the expanding exhaust hot gas are being considered in the thermal analysis. The gas radiation is a function of the combustion products and their density and pressure. As a result, over 95% of the heat produced in the exhaust plume is within the intrinsic core of the exhaust plume. The gas that expands

toward the Prandtl-Meyer expansion limit has very low pressure and density and does not generate significant heat. However, the radiation from the hot engine nozzle produces major heating. As a result, the radiation shielding for the adjacent components on the SM might be required based on further analysis.

Table 4 Main engine exhaust plume radiation heat flux (100 km, $\alpha = 0^o$)

$[r_1,r_2]$ (m)	height (m)	volume (m^3)	surface area (m^2)	Le (m)	$p_{CO2}Le$ (atm-ft)	$p_{H2O}Le$ (atm-ft)	ε_g	T_g (K)	q (kw)
[1.1,5.6]	10.1	410	233	4.89	0.0011	0.00275	0.0008	850	5.5
[5.6,7.0]	5.4	676	221	5.7	0.000688	0.0017	0.0005	600	0.8
[7.0,8.5]	7	1325	348.6	7.265	0.00029	0.0007	0.00025	500	0.3

Table 5 Main engine exhaust plume radiation heat flux (400 km altitude and above)

$[r_1,r_2]$ (m)	height (m)	volume (m^3)	surface area (m^2)	Le (m)	$p_{CO2}Le$ (atm-ft)	$p_{H2O}Le$ (atm-ft)	ε_g	T_g (K)	q (kw)
[4,10]	10.8	1764.3	543.4	7.774	0.00066	0.001635	0.0004	850	6.43
[10,15]	13.2	6566	1108.6	12.333	0.000456	0.001128	0.00018	550	1.03

3. Thermal analysis on the service module components

The thermal analysis is performed using Thermal Desktop. The major components in the model are the SM main engine, solar panels in a stowed position, and the radiator panel. Inside the main engine, both convection and radiation boundary conditions are imposed. The exhaust plume was modeled as a series of connected parabolas that are defined based on the radius and height listed in Table 3, and the corresponding heat flux is applied to each section of the parabola. The total heat radiated from the exhaust plume was 6.6 kW of heat for the 100 km altitude and 7.46 kW for the 400 km altitude. Thermal Desktop was used to calculate the view factors between the geometry and the resulting temperatures. The stowed solar panel whose optical properties used here is an emissivity of 0.9 and solar absorptivity of 0.9. The ten layers of MLI insulation comprises a 3.0-mil-thick black Kapton outer layer, and four layers of double-aluminized Kapton, and five layers of double-aluminized Mylar with Dacron netting spacers. Its effective emmisivity is 0.05 and solar absorbtivity is 0.14 [5]. The five layer design comprises an outer layer of double-aluminized Kapton and four layers of double-aluminized Mylar with Dacron spacers. Its effective emmisivity is 0.1 and solar absorbtivity is 0.14 [5]. Three configurations of CEV SM (LM 604, 605, and 606) are considered. For each configuration, three cases including no insulation, 5 layers of MLI, and 10 layers of MLI are studied by changing the optical properties on the solar panel

with its corresponding insulation. On each surface of the solar panel, two mesh elements are used in the model for the 604 configuration; three mesh elements are used in the model for the 605 and 606 configurations. More mesh elements can be used if it is necessary. The ambient temperature is assumed to be at 0 K.

For the CEV 604 configuration, the computed temperature contour at t = 0.5 hr with five layers of MLI is plotted in Figure 4 to show a representative temperature distribution on the thermal model. Furthermore, the time history of the temperature at the center of two mesh elements on the solar panel surface is plotted in Figure 5 for different thermal insulations. It can be seen that, with no insulation, it takes about 0.2 hr for the solar panel to reach the steady state at 650 ^{o}F, which exceeds the safe-operating limit of the solar panel. The temperature reaches 575 ^{o}F for using a 5-layer MLI blanket and 420 ^{o}F for using a 10-layer MLI blanket at t = 0.5 hr. The steady state has not been reached yet.

For the CEV 605 configuration, the computed temperature contour at t = 0.5 hr with 10 layers of MLI is plotted in Figure 6, while the time history at the center of the three mesh elements on the solar panel surface with different insulations is plotted in Figure 7. Similarly, the maximum temperature on the solar panel could reach 680 ^{o}F within 0.3 hr if there is no insulation on the solar panel. The maximum temperature could drop to 625 ^{o}F using 5 layers of MLI and 425 ^{o}F using a 10-layer MLI blanket at t = 0.5 hr.

For the CEV 606 configuration, the computed temperature contour at t = 0.5 hr with five-layer MLI is plotted in Figure 8 and the corresponding time history is plotted in Figure 9. The solar panel is farther away from the engine nozzle and most of the area is blocked by the radiator panel compared with the 604 and 605 configurations. Without a MLI blanket, the maximum temperature is 375 ^{o}F at t = 0.3 hr and reaches steady state. With a 5-layer MLI, the maximum temperature is 230 ^{o}F and 145 ^{o}F for 10 layers of MLI at t = 0.5 hr.

In summary, the CEV 606 configuration provides the best thermal environment from the main engine for the solar panel. Both the 604 and 605 configurations have similar thermal conditions and need more layers of MLI blanket.

Acknowledgments

References

[1]. F.P. Incropera and D.P. DeWitt, "Fundamentals of heat and mass transfer," 5th Ed., John Wiley & Sons Inc., 2002.
[2]. R. Siegel and J.R. Howell, "Thermal radiation heat transfer," 3rd Ed., Hemisphere Publishing Corporation, Washington, 1992.
[3]. F.S. Simmons, "Rocket exhaust plume phenomenology," p. 25, Aerospace Corporation, El Segundo, 2000.
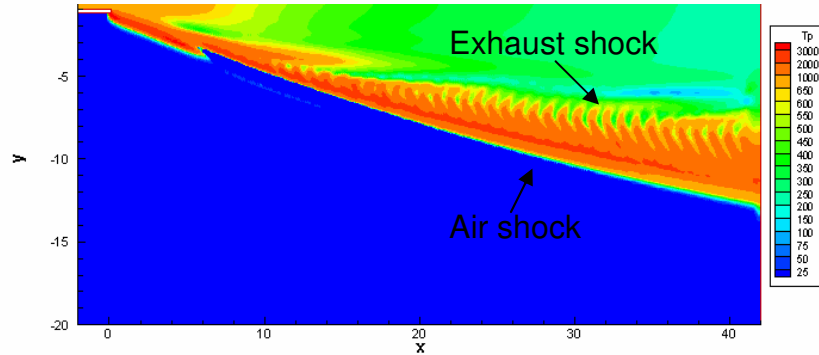[4]. M.A. Saad, "Compressible fluid flow," Prentice-Hall Inc., 1995.

[5]. D.G. Gilmore, "Spacecraft thermal control handbook," Volume I: fundamental technologies, 2nd Ed., The Aerospace Press, El Segundo, California, 2002.
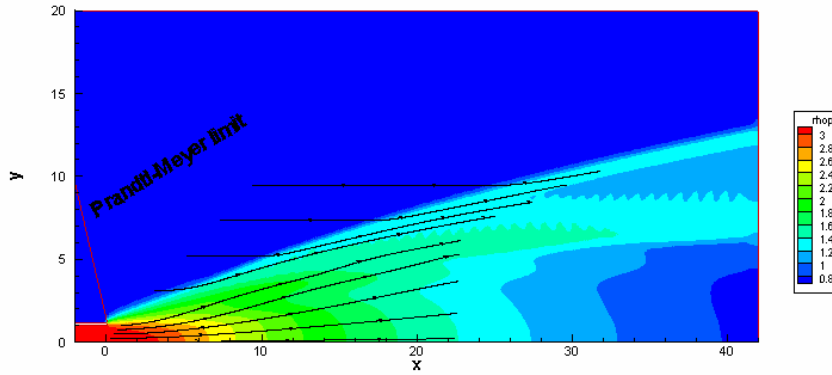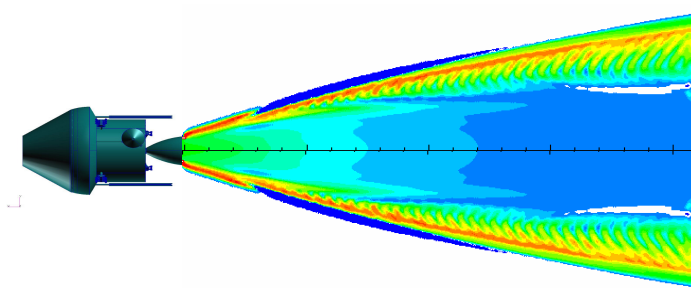
(a) Log$_{10}$ ρ contour (Kg/cm^3)
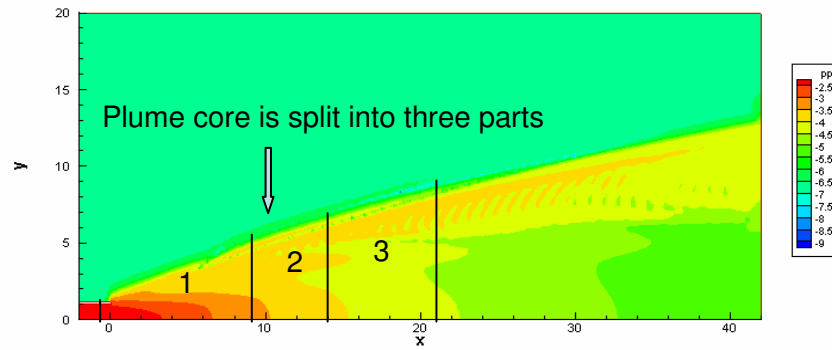
(b) Log$_{10}$ p contour (atm)

(c) T contour (K)

(d) Plume relative to CEV

Figure 2 Plume at the altitude of 100 km with α = 0°.

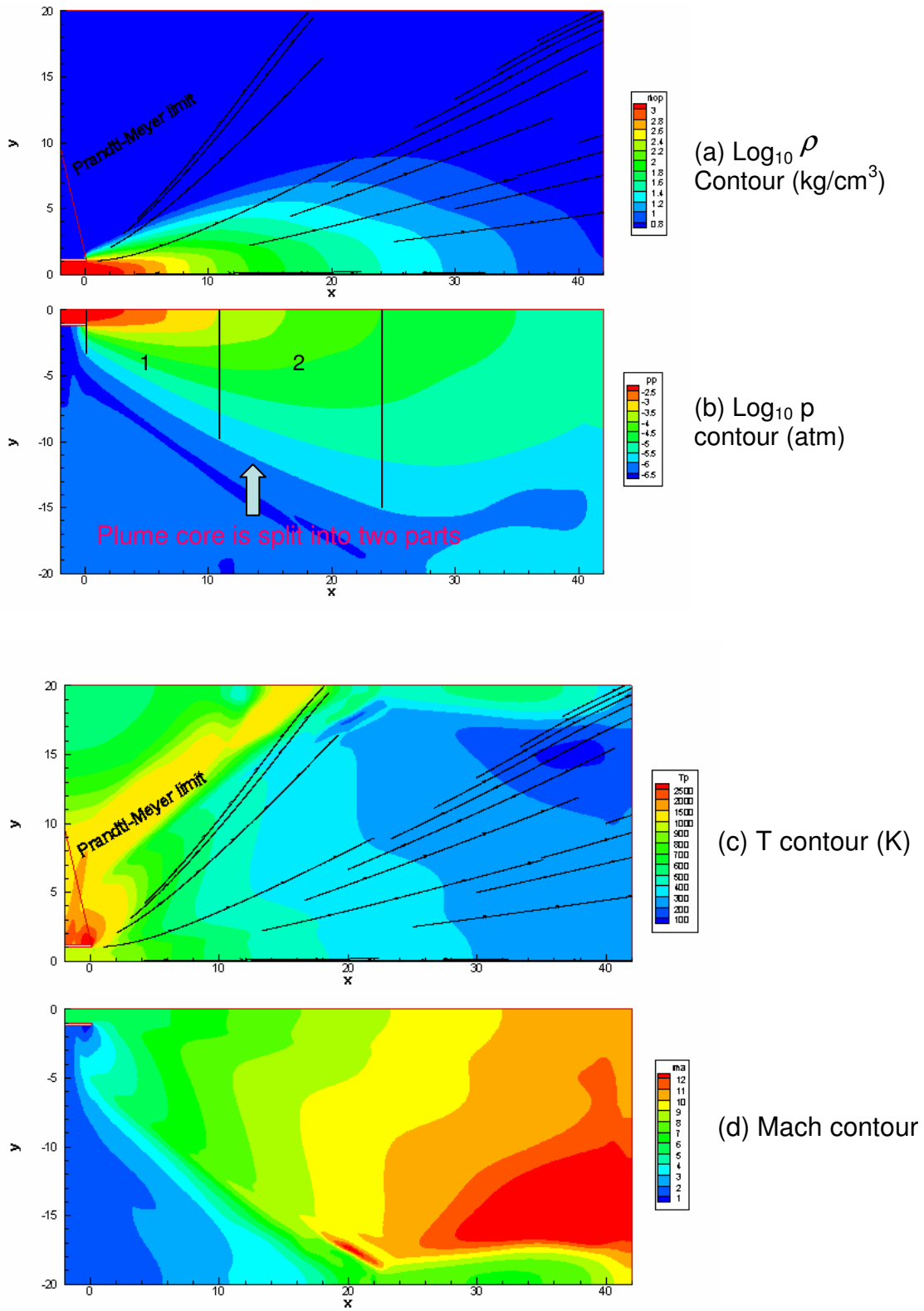(a) Log$_{10}$ ρ Contour (kg/cm^3)

(b) Log$_{10}$ p contour (atm)

(c) T contour (K)

(d) Mach contour

Figure 3 Plume at the altitude of 400 km and above.
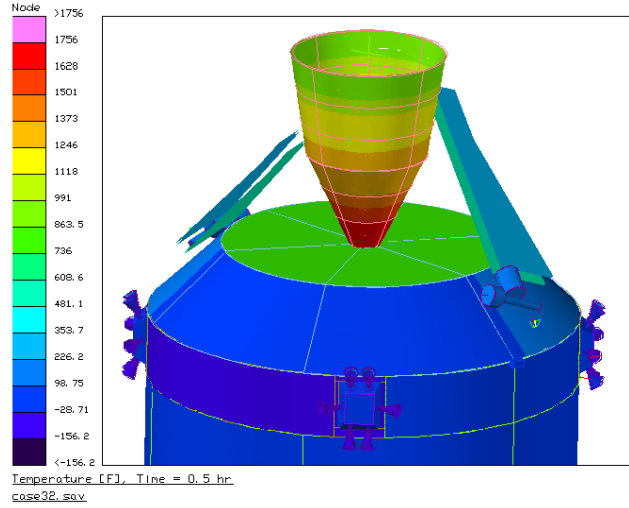
Figure 4 Temperature contour at t = 0.5 hr for the 604 configuration with 5-layer MLI blanket.
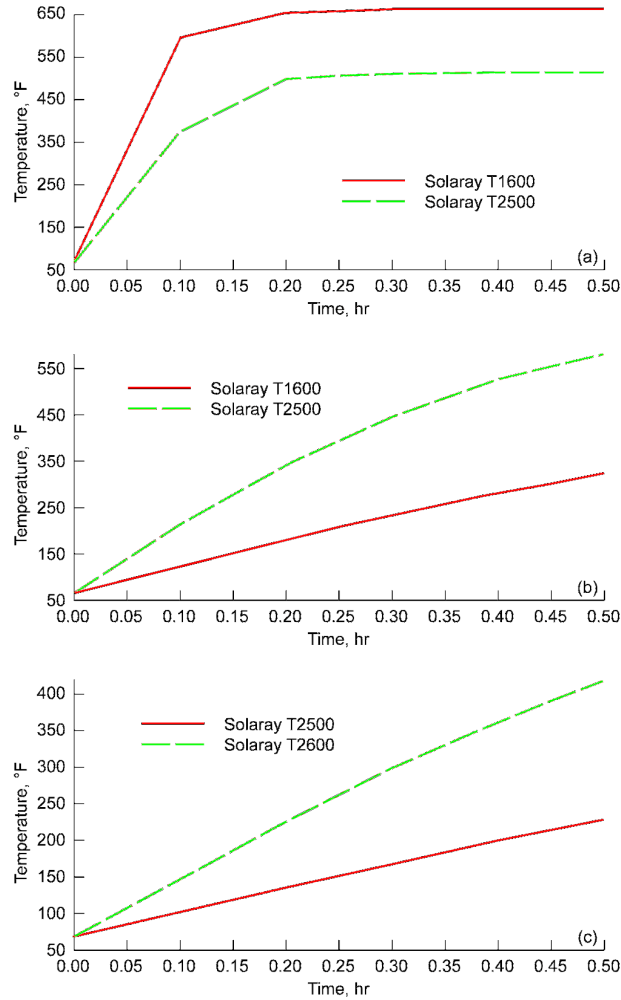
Figure 5 Time history of temperature at the center of two mesh elements on solar panels for the 604 configuration. (a) With no insulation, (b) Five-layer MLI, (c) Ten-layer MLI.
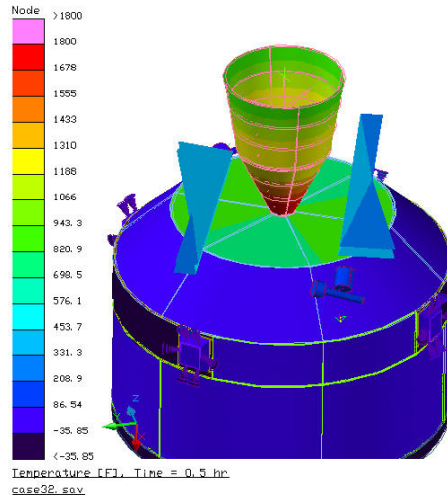
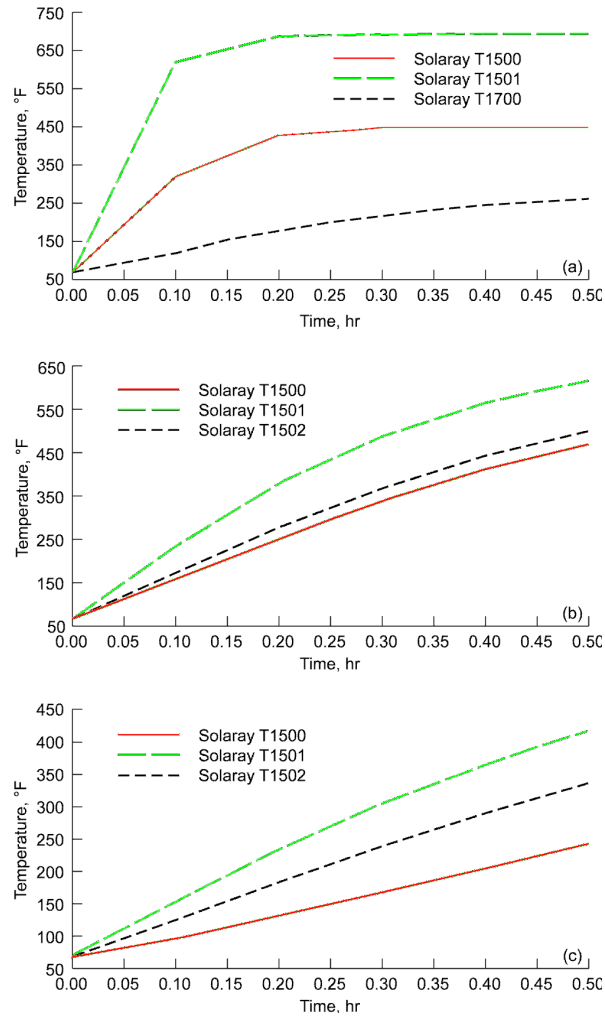**Figure 6 Temperature contour at t = 0.5 hr for the 605 configuration with 10-layer MLI blanket.**

Figure 7 Time history of temperature at the center of three mesh elements on solar panels for the 605 configuration. (a) With no insulation, (b) Five-layer MLI, (c) Ten-layer MLI.
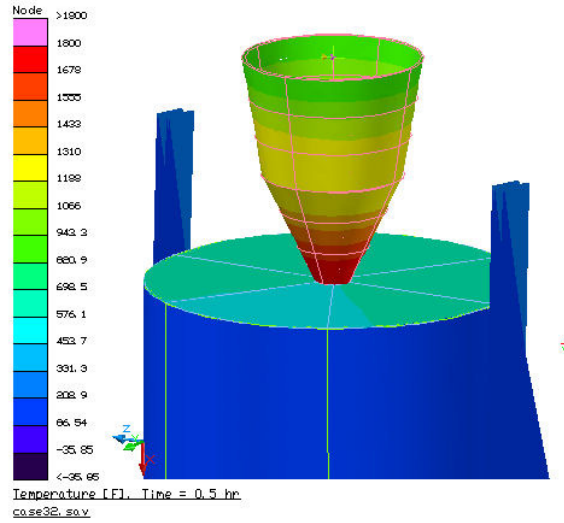
Figure 8 Temperature contours at t = 0.5 hr for the 606 configuration with 5-layer MLI blanket.
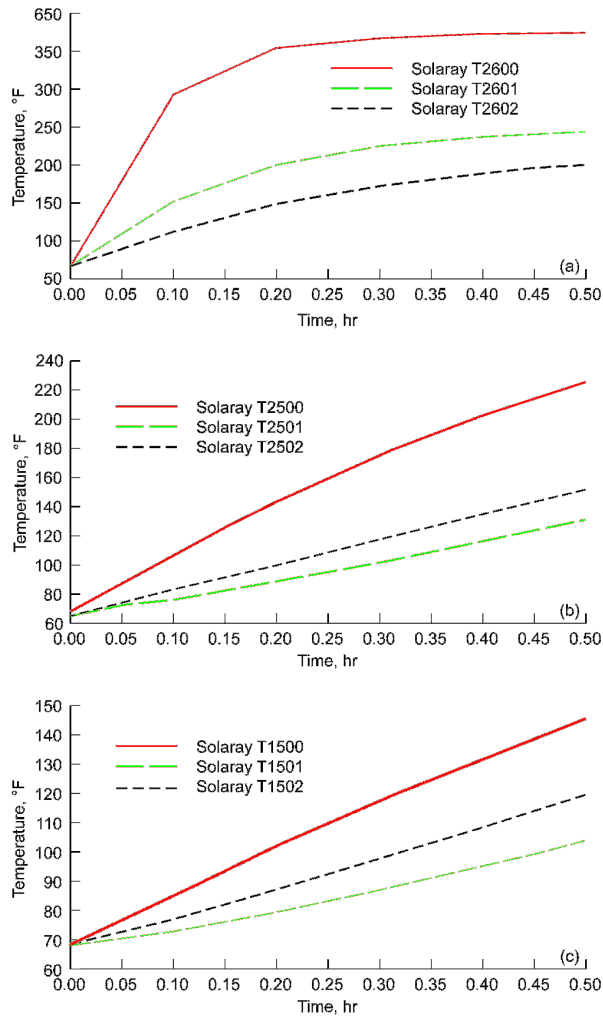

Figure 9 Time history of temperature at the center of three mesh elements on solar panels for the 606 configuration.   (a) With no insulation, (b) Five-layer MLI, (c) Ten-layer MLI.

11